Role of the South China Sea in Regulating the North Pacific Double-Gyre System

HAIYUAN YANG AND LIXIN WU

Physical Oceanography Laboratory/CIMST, Ocean University of China and Qingdao National Laboratory for Marine Science and Technology, Qingdao, China

SHANTONG SUN

Scripps Institution of Oceanography, University of California, San Diego, La Jolla, California

ZHAOHUI CHEN

Physical Oceanography Laboratory/CIMST, Ocean University of China and Qingdao National Laboratory for Marine Science and Technology, Qingdao, China

(Manuscript received 13 December 2016, in final form 9 April 2017)

ABSTRACT

The role of the South China Sea (SCS) in regulating the North Pacific circulation is investigated using a two-layer quasigeostrophic (QG) model. The double-gyre circulations in the North Pacific with and without the SCS are compared and analyzed. It is found that the SCS acts as a sink of both potential vorticity (PV) and energy in the Pacific–SCS system for the mean state. Consequently, the Kuroshio and the upstream Kuroshio Extension (KE) are weaker in the presence of the SCS. Moreover, the eddy activity is also lower in the North Pacific Ocean because the barotropic instability is suppressed for a weaker circulation. In terms of low-frequency variations at interannual to decadal time scale, the presence of the SCS is found to enhance the variability of the latitudinal position and intensity of the KE jet. This is explained by a positive feedback process that is associated with the negative correlation between the inertia of the Kuroshio and its intrusion into the SCS.

1. Introduction

Interaction between the open ocean and marginal seas is an important process in the global ocean, playing an important role in regulating the potential vorticity (PV), energy, and heat balance of the circulation system. For the marginal seas, exchange of PV and mass with the open ocean would affect their thermocline structures and therefore regulate the circulation characteristics (Helfrich and Pratt 2003). For example, the pattern of South China Sea (SCS) deep circulation can be explained by the intrusion of high PV water from the Pacific (Wang et al. 2011; Lan et al. 2013). For the open ocean, interaction with the marginal seas may also significantly influence its circulation pattern and eddy activity (e.g., Kida et al. 2009). In the Atlantic Ocean, for instance, the establishment of the Azores Current is attributed to the mass compensation for water exchange between the Atlantic Ocean and the Mediterranean Sea (Kida et al. 2008).

In the North Pacific Ocean, interaction between the SCS and the Pacific Ocean mainly takes place at the Luzon Strait associated with the Kuroshio intrusion into the SCS (Xue et al. 2004; Gan et al. 2006; Liang et al. 2008; Nan et al. 2011). During this process, the main axis of the Kuroshio flows into the SCS through the Balintang Channel and flows out of the SCS subsequently through the Bashi Channel, making an important contribution to the exchange of PV, energy, and mass between these two basins. Previous studies suggest that the Kuroshio intrusion can significantly regulate the mean circulation and oceanic variability in the northern SCS (Hu et al. 2000; Liu et al. 2008; Nan et al. 2015). It is also found that the Kuroshio intrusion can exert crucial impacts on the downstream Kuroshio. For example, the path of the Kuroshio to the northeast of Taiwan is found

Corresponding author: Haiyuan Yang, yanghaiyuan@ouc.edu.cn

DOI: 10.1175/JPO-D-16-0272.1

to be largely influenced by its mean-state trajectory at the Luzon Strait (Hsin et al. 2013). A looping current at the Luzon Strait is associated with a larger eastward current in the northern Luzon Strait and would generate an offshore displacement of the Kuroshio from Taiwan. In contrast, a relatively straight path of the Kuroshio near Luzon tends to make the Kuroshio closer to the Taiwan Island. This will further influence the intensity of frontal eddies southeast of Taiwan (Jing and Li 2003; Kuehl and Sheremet 2009), the upwelling process northeast of Taiwan (Wu et al. 2008), and the Kuroshio intrusion into the East China Sea (Wu et al. 2014). In addition, the water from the SCS can join the Kuroshio around the southern tip of Taiwan (Liang et al. 2003), affecting the biochemistry of the Kuroshio (Chang et al. 2009). As suggested by Yang and Price (2007), interaction between two ocean basins through a channel may cause a basin-scale adjustment process. However, all those studies working on the North Pacific have been focused on the local circulation and the Kuroshio itself, but determining the role of the SCS in regulating the entire North Pacific double-gyre circulation remains elusive.

The circulation in the North Pacific is characterized by a double-gyre system, which is a classical topic in ocean circulation dynamics (Pedlosky 1996). In this system, western boundary currents play an irreplaceable role in the mass conservation, energy/PV budget, and heat transport. For the mean state, western boundary currents are the mass compensation for the ocean currents in the interior ocean (Stommel 1948). Moreover, advection of PV by the western boundary currents maintains the strong recirculation (Marshall and Nurser 1986; Ierley 1987; Cessi 1988; Marshall and Marshall 1992), which further regulates the state of the eastward jet and gyre system (Cessi 1988; Jiang et al. 1995; McCalpin and Haidvogel 1996). In addition to the mean state, previous studies also highlighted the role of western boundary currents in regulating the temporal variability in the circulation system. Based on both observations and model simulations, it is found that the double-gyre circulation is a highly nonlinear system with energetic eddies, and low-frequency variability of this system is characterized by changes in the meridional position and strength of the oceanic eastward jet (Dewar 2003; Taguchi et al. 2007; Berloff et al. 2007a). Berloff and McWilliams (1999b) reported that the eastward jet can be disrupted and broadened in the regime with a strong, local instability of the western boundary current. Chang et al. (2001) found that transition of the double-gyre system from high-energy state to low-energy state is accompanied by the rapid change of western boundary currents. Berloff et al. (2007a) examined this low-frequency evolution in detail through PV budget analysis and concluded that change of lateral dissipation associated with western boundary currents plays a damping role in this evolution. Overall, these studies implied the possibility that presence of the SCS may regulate the double-gyre system in the North Pacific Ocean, given the role of the SCS in influencing the upstream Kuroshio.

By using a two-layer quasigeostrophic (QG) model, the role of the SCS in regulating the North Pacific circulation is studied in this paper in terms of both the mean circulation and its temporal variability. Here, we focus on the intrinsic ocean dynamics. The external effects, such as the wind forcing, bottom topography, and the shape of the basin will not be considered. This paper is organized as follows: Section 2 gives a brief description of the QG model. In section 3, a detailed examination of model results is presented, followed by analysis of the relevant mechanism in section 4. This paper is summarized in section 5.

2. Model

In this study, we use a two-layer QG model with the governing equations (Pedlosky 1987)

$$\frac{\partial q_1}{\partial t} + J(\psi_1, q_1) = \frac{f_0}{H_1} W + A_H \nabla^4 \psi_1, \quad \text{and} \tag{1a}$$

$$\frac{\partial q_2}{\partial t} + J(\psi_2, q_2) = A_H \nabla^4 \psi_2 - \gamma \nabla^2 \psi_2 . \tag{1b}$$

Here, q_i represents PV, ψ_i is the streamfunction, $A_H = 150\,\mathrm{m^2\,s^{-1}}$ is the horizontal eddy viscosity coefficient, $\gamma = 10^{-7}\,\mathrm{s^{-1}}$ represents the linear bottom friction coefficient, and H_i indicates the mean layer thickness, where the subscript i ($i = 1, 2$) is the layer index, starting from the top layer. The symbol ∇^2 is the horizontal Laplacian operator, and $J(a, b) = a_x b_y - a_y b_x$ is the Jacobian operator. The term q_i is connected with ψ_i through the coupled elliptic equations:

$$q_1 = \nabla^2 \psi_1 + \frac{f_0^2}{g' H_1}(\psi_2 - \psi_1) + \beta y, \quad \text{and} \tag{2a}$$

$$q_2 = \nabla^2 \psi_2 + \frac{f_0^2}{g' H_2}(\psi_1 - \psi_2) + \beta y, \tag{2b}$$

where $g' = 0.03\,\mathrm{m\,s^{-2}}$ represents the reduced gravity ($g' = g\Delta\rho/\rho$). During the numerical calculation, an eigenmode decomposition method is used to decouple these equations (Zhong et al. 2016). The beta-plane approximation is adopted with $f_0 = 7 \times 10^{-5}\,\mathrm{s^{-1}}$ and $\beta = 2 \times 10^{-11}\,\mathrm{m^{-1}\,s^{-1}}$. The model domain in this study includes two flat-bottom square basins that are

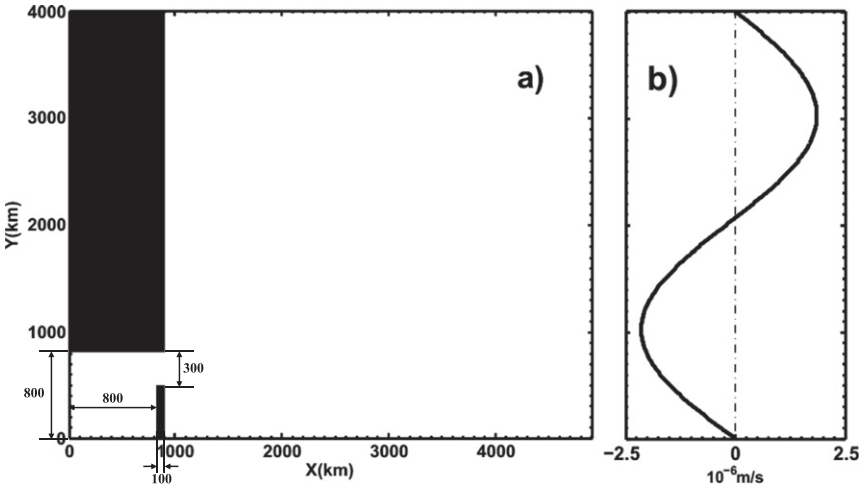

FIG. 1. (a) The model domain used in this study. The black (white) areas denote the land (ocean). The size of the basin and channel is indicated. (b) Ekman pumping velocity W plotted as a function of y, which is defined in Eq. (3). The zero position of Ekman pumping velocity is plotted as a dashed–dotted line.

connected by a narrow strait, representing the western Pacific and the SCS north of 15°N (Fig. 1a). The sizes of the North Pacific, the northern SCS deep basin, and the Luzon Strait are set to be $L = 4000\,\text{km}$, $l = 800\,\text{km}$, and $l_s = 300\,\text{km}$, respectively. The depth of the upper layer H_1 is 300 m. The depth of the bottom layer H_2 is 3700 m for the Pacific Ocean and 1700 m for the SCS and the Luzon Strait, close to observations (Wang et al. 2013).

The wind forcing W in the model is imposed as vertical Ekman pumping velocity, which has a double-gyre pattern in the modeled Pacific Ocean (Fig. 1b):

$$W = -w_0\left[\sin\left(\frac{2\pi}{L_y}y\right) + 0.1\sin\left(\frac{\pi}{L_y}y\right)\right], \qquad (3)$$

where the amplitude w_0 is chosen as $2 \times 10^{-6}\,\text{m s}^{-1}$ following previous QG studies (Sun et al. 2013), which is comparable to observations (Risien and Chelton 2008). The meridional distance between the zero Ekman pumping line and the Luzon Strait is about 1500 km, comparable to observation as well (Risien and Chelton 2008). With this wind forcing setting, the Sverdrup transport is about 30 Sv ($1\,\text{Sv} \equiv 10^6\,\text{m}^3\,\text{s}^{-1}$) in the subtropical gyre, which is smaller than reality (~40 Sv; Isobe and Imawaki 2002) because of the narrow Pacific basin in the model. The forcing is set to be slightly asymmetric with respect to the midlatitude of the basin in order to avoid the artificial symmetrization of the gyres (Berloff and McWilliams 1999a). In the reference run, the forcing is only applied in the Pacific Ocean, and it is confirmed by diagnosing that the role of wind forcing in the SCS is negligible (not shown).

The boundary conditions used here are the no normal flow condition

$$\psi_i = \psi_i(t) \qquad (4)$$

and partial-slip lateral boundary condition (Haidvogel et al.1992)

$$\frac{\partial^2\psi_i}{\partial n^2} + \alpha\frac{\partial\psi_i}{\partial n} = 0, \qquad (5)$$

where n represents the outward unit normal vector. In this study, the dynamical streamfunction, which is defined as the difference between streamfunction and streamfunction at the boundary (Cessi and Primeau 2001),

$$\psi_{\text{dynamic}} = \psi - \psi_{\text{boundary}}, \qquad (6)$$

is used to determine the intergyre boundary between two gyres. In the reference case, $\alpha = 0.05\,\text{km}^{-1}$ lies between the no-slip lateral boundary condition $\alpha \to \infty$ and the free-slip boundary condition $\alpha = 0$. In addition, the mass conservation equation (McWilliams 1977)

$$\frac{\partial}{\partial t}\iint(\psi_1 - \psi_2)\,dA = 0 \qquad (7)$$

is adopted, where dA is the elementary area.

The spatial resolution δ_s in this study is 10 km. With our parameter settings, the baroclinic deformation

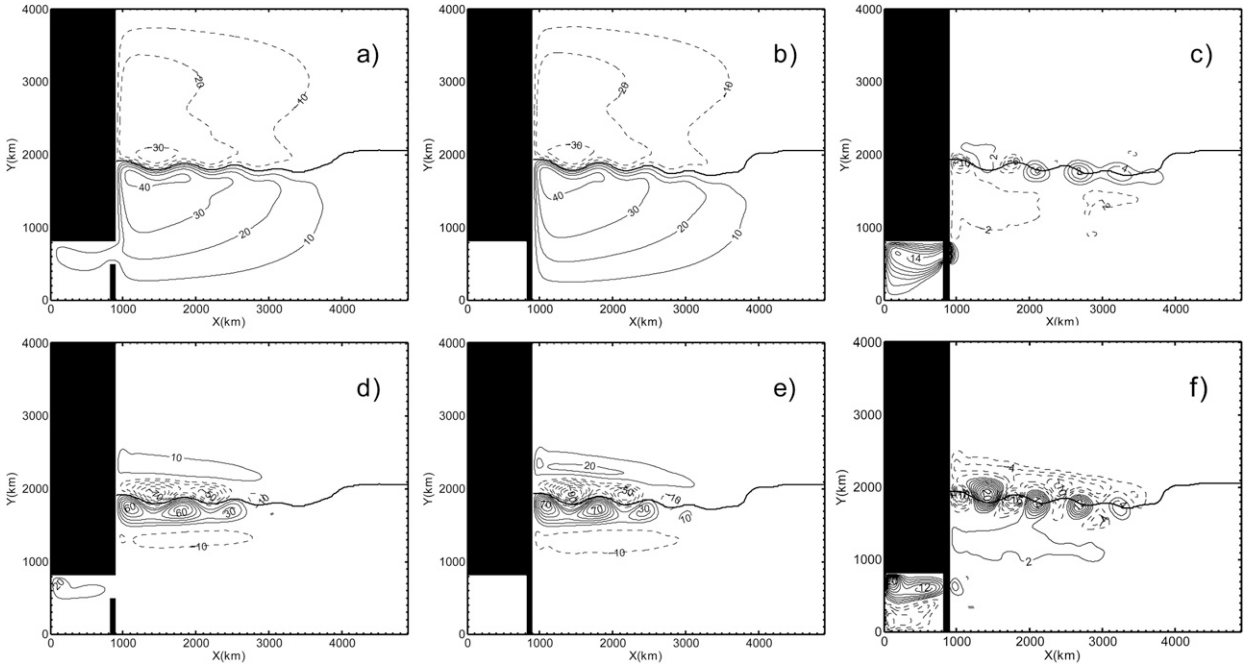

FIG. 2. (top) Mean upper-layer streamfunctions (Sv) for (a) OL, (b) CL, and (c) their difference (OL minus CL). (bottom) As in (top), but for the bottom-layer streamfunctions. Contour interval (CI) is 10 Sv in (a), (b), (d), and (e) and 2 Sv in (c) and (f).

radius $R_d = \sqrt{g'H_1H_2/(H_1 + H_2)}/f_0$ is 41 km, which can be resolved by four model grid points. The wave speed of the first baroclinic long Rossby wave $C_R = \beta R_d^2 = 3.4\,\mathrm{cm\,s^{-1}}$ and is consistent with the estimation in the midlatitude Pacific Ocean (Chelton et al. 2011).

In this study, two simulations are performed: the ''opened Luzon'' simulation (OL) and the ''closed Luzon'' simulation (CL). In each case, the model is first integrated using the leapfrog time-stepping algorithm from rest to a statistical equilibrium, which is determined by the total kinetic energy. After a spinup for 100 years from a state of rest, each case is integrated for another 175 years, and the results are saved every 8 days for analysis in sections 3 and 4. For more details about the numerics of this model, readers are referred to Mu et al. (2011) and Zhong et al. (2016).

3. Influence of the SCS on the double-gyre system

a. Mean state

Before exploring the influence of the SCS on the North Pacific circulation system, we first examine the model's performance in the North Pacific region. Figures 2a and 2b show the mean upper-layer streamfunctions derived from OL and CL, respectively. Although the model is highly idealized, it appears to be able to reproduce the basic features of the North Pacific double-gyre system, with a cyclonic gyre in the north, an anticyclonic gyre in the south, and a strong eastward jet between the two gyres. In both cases, the total transport of the Kuroshio at $y = 1000$ km (25°N) is around 30 Sv, which is close to the Sverdrup transport at this latitude. However, it is smaller than the real transport of the Kuroshio across the PN line in the East China Sea (40 Sv; Isobe and Imawaki 2002), which is mainly caused by the narrow Pacific basin in the model. The transport of the Oyashio at $y = 3000$ km (45°N) is around 23 Sv and is comparable to both the Sverdrup transport at this latitude (26 Sv) and observations (Qiu 2001). After separating from the western boundary, the offshore Kuroshio enters the North Pacific Ocean and forms the Kuroshio Extension (KE), which is characterized with obvious quasi-stationary meanders and a pair of counterrotating recirculation gyres on its flank (Fig. 2). The total transport of the recirculation south of KE in QG model reaches 100 Sv and is generally comparable to that from observations (Qiu 2001). It should be noted that KE in this study is a confluence of Kuroshio and Oyashio, thus part of the modeled KE is driven by subpolar winds, which is different from reality (Yasuda 2003). In section 4c, we will discuss the case in which KE and Oyashio Extension are separated. In the OL case, an anticyclonic Loop Current is observed in the northern SCS, which is caused by the Kuroshio intrusion in the upper layer and resembles the patterns in previous QG

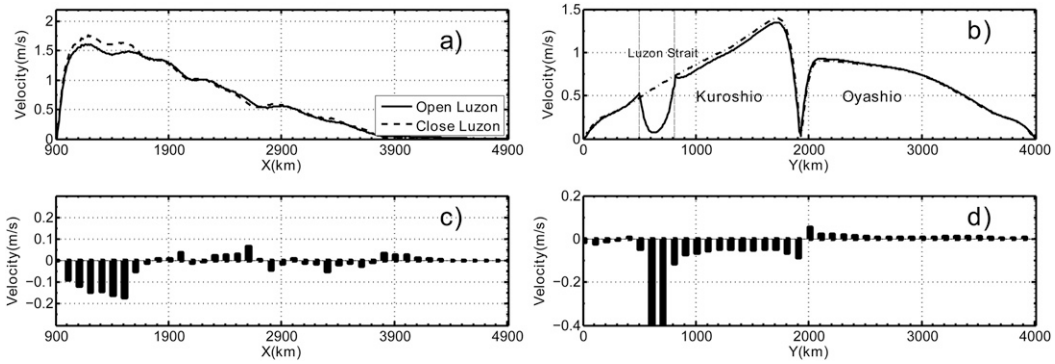

FIG. 3. (a) Time-mean velocity ($m\,s^{-1}$) of KE in two cases [OL (solid); CL (dashed)]. (b) As in (a), but for the velocity of the western boundary currents. (c) Velocity difference of KE between the two cases (OL minus CL). (d) As in (c), but for the western boundary currents. Values greater than $0.4\,m\,s^{-1}$ are not presented.

studies (Mu et al. 2011; Zhong et al. 2016) and from theoretical calculation (Sheremet 2001). The transport of the Loop Current is 15 Sv and is close to the result of Mu et al. (2011). Unlike the upper ocean, the bottom-layer circulation is mainly confined to the KE regions (Figs. 2d,e), in accord with previous studies (Dewar 2003; Berloff et al. 2007a). In the following, we will estimate the role of the SCS in regulating this system in terms of both its mean state and variability.

Differences of the time-mean upper-layer streamfunctions between the two cases are shown in Fig. 2c. Negative values are found in the subtropical region ($900 < x < 1700$ km and $1000 < y < 2000$ km), implying a weaker subtropical gyre when the Luzon Strait is open. To clarify this in more detail, we calculate the time-mean velocity of the upper-layer KE and western boundary current in both cases (Fig. 3). Here, the velocity of the KE plotted in Fig. 3a is the zonal velocity along the zero time-mean dynamical streamfunction line (thick black contour in Figs. 2a,b). The velocity of the western boundary current plotted in Fig. 3b is the maximum meridional velocity within $900 < x < 1000$ km. Along the KE, the time-mean velocity reaches its maximum $1.6\,m\,s^{-1}$ near the western boundary and then decreases toward the east (Fig. 3a). Compared to CL, the velocity of KE in OL is weaker by about 10% between $900 < x < 1700$ km (Fig. 3c). Along the western boundary currents, the velocity presents a bimodal structure with the maximums located at the latitudes of the two recirculations (Fig. 3b). Comparisons between OL and CL indicate that the velocity of Kuroshio in OL is reduced by about 8% between $800 < y < 1800$ km, while differences of the Oyashio between these two cases are insignificant (Fig. 3d). In the bottom layer, we find the overall impact of the SCS is similar to that in upper layer; the recirculation gyres are weaker in OL than in CL (figure not shown).

b. Variability

Estimation of the perturbation kinetic energy (PKE) is a direct way to measure the variability of ocean circulation. In the upper layer, PKE is defined as

$$\mathrm{PKE} = \frac{1}{2}\mathbf{U}'^2 = \frac{1}{2}(u_1', v_1')^2 = \frac{1}{2}\left(-\frac{\partial\psi_1'}{\partial y}, \frac{\partial\psi_1'}{\partial x}\right)^2. \quad (8)$$

Here, prime indicates anomaly; $\mathbf{U} = (u_1, v_1)$ is the upper-layer horizontal velocity, and ψ_1' is upper-layer streamfunction anomaly. According to previous studies, both the mesoscale and low-frequency variability are energetic in the ocean (Berloff and McWilliams 1999a). To respectively characterize them, we decompose the anomalous velocity field $\mathbf{U}'$ for computing the PKE into high-frequency $\mathbf{U}'_{\mathrm{high}}$ and low-frequency $\mathbf{U}'_{\mathrm{low}}$ components with a cutoff period of 500 days, that is,

$$\mathbf{U}' = \mathbf{U}'_{\mathrm{high}} + \mathbf{U}'_{\mathrm{low}}. \quad (9)$$

In this study, the cutoff period is chosen to be 500 days based on the eddy time scales following Berloff et al. (2007a). The value of $\mathbf{U}'_{\mathrm{low}}$ is extracted from $\mathbf{U}'$ through 500-day low-pass filtering, and $\mathbf{U}'_{\mathrm{high}}$ is obtained through 500-day high-pass filtering. Moreover, we have changed this cutoff frequency successively from 400 to 800 days and found the results are not sensitive to the selection. The PKE corresponding to $\mathbf{U}'_{\mathrm{high}}$ peaks at the KE region, especially around $2000 < x < 3000$ km (Fig. 4a). In the OL case, the area-mean PKE in the vicinity of KE is reduced by about 10% compared to CL, implying weaker variability in that region (Fig. 4b). The PKE calculated from $\mathbf{U}'_{\mathrm{low}}$ depicts similar patterns at the KE region with maximum values that flank the KE jet between $1000 < x < 1600$ km (Fig. 4c). Compared to the CL case, the low-frequency variability within the KE area is stronger by 6% in the OL case, which can be

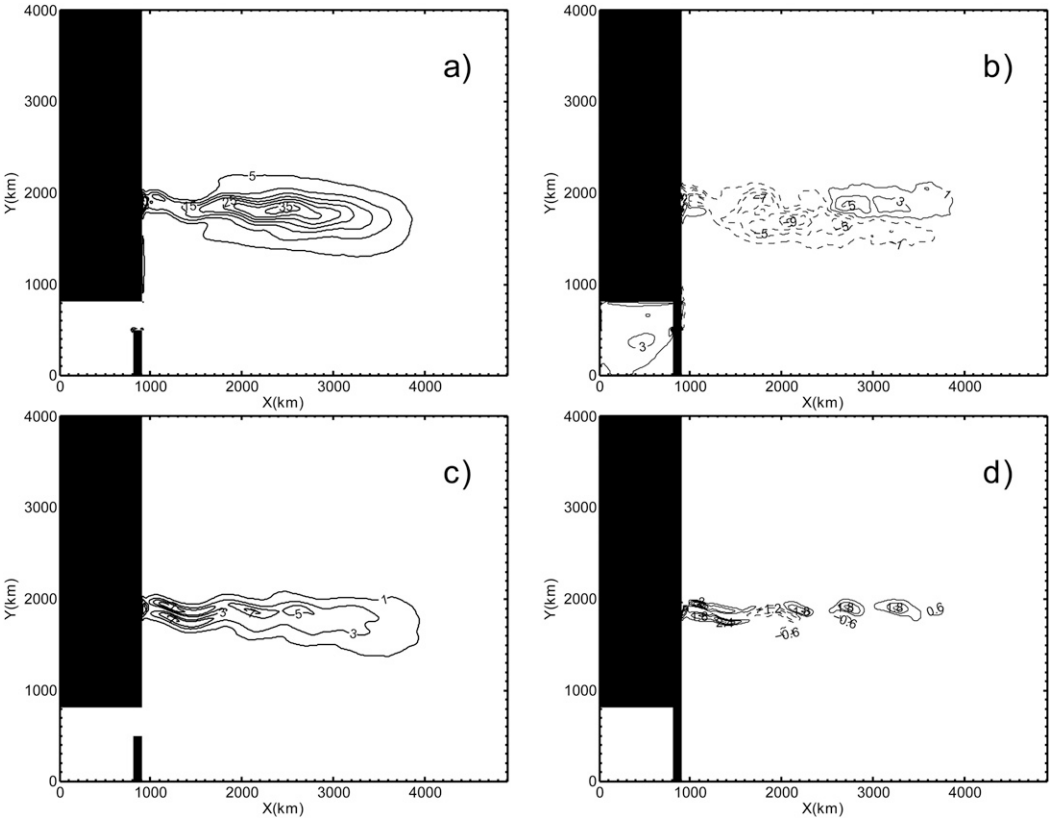

FIG. 4. (a) $0.5\mathbf{U}'^2_{\text{high}}$ in the OL case ($0.01\,\text{m}^2\,\text{s}^{-2}$; CI = $0.05\,\text{m}^2\,\text{s}^{-2}$) and (c) differences between the OL and CL cases (OL minus CL; CI = $0.02\,\text{m}^2\,\text{s}^{-2}$). (b) As in (a), but for $0.5\mathbf{U}'^2_{\text{low}}$ (CI = $0.02\,\text{m}^2\,\text{s}^{-2}$). (d) As in (c), but for $0.5\mathbf{U}'^2_{\text{low}}$ (CI = $0.006\,\text{m}^2\,\text{s}^{-2}$).

inferred from the positive values along the KE axis (Fig. 4d).

To better understand the physics of the high-frequency and low-frequency components of variabilities, we carry out an empirical orthogonal function (EOF) analysis for the OL case. For high-frequency variability, the analysis is applied to the 500-day, high-pass filtered, upper-layer streamfunction anomaly. The leading 10 EOF modes explain over 60% of the total variance. Their spatial patterns are all characterized by a vortex train in the vicinity of KE (e.g., Fig. 5a). The corresponding principal components (PCs) are highly

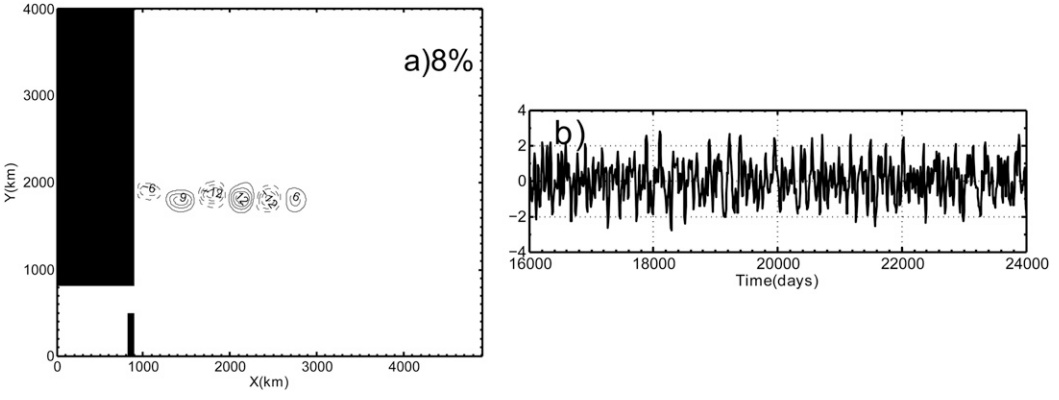

FIG. 5. (a) First EOF mode of the 500-day high-pass streamfunction anomaly of the upper layer in OL (Sv; CI = 3 Sv). The value 8% in (a) refers to the explained variance of the first EOF mode. (b) Normalized PC of first EOF mode during model days 16 000–24 000.

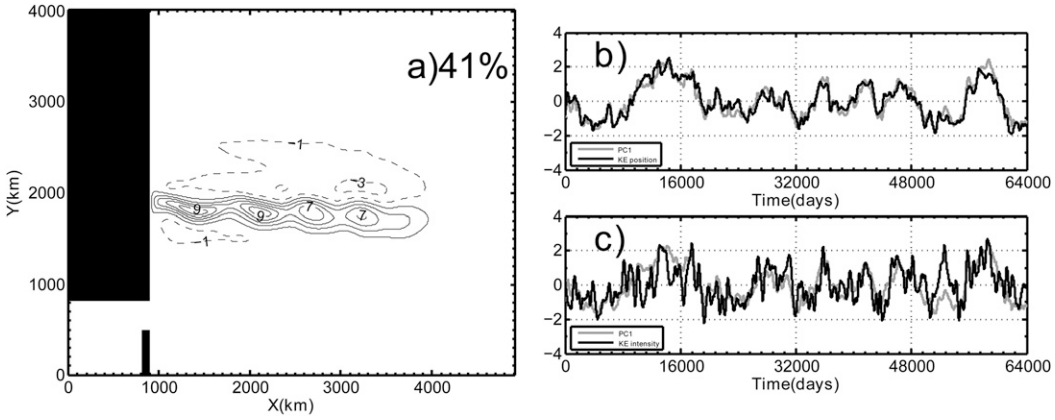

FIG. 6. (a) The first EOF mode of the 500-day low-pass streamfunction anomaly of the upper layer in OL (Sv; CI = 2 Sv). The value 41% in (a) refers to the explained variance of the first EOF mode. (b) Normalized PC of first EOF mode (gray) and normalized KE position index (black). (c) Normalized PC of first EOF mode (gray) and normalized KE intensity index (black).

variable with time scales between 150 and 200 days (Fig. 5b). We have compared these modes with inviscid linear basin modes (Pedlosky 1987). The linear basin modes are all characterized by wavelike patterns in the interior ocean (Pedlosky 1987, his Fig. 3.25.3, p. 148), which is different from the EOF modes in Fig. 5a. Moreover, the periods and spatial scales of the vortices do not match the governing dispersion relationship of the linear basin modes [Pedlosky 1987, his Eq. (3.25.16), p. 147]. Therefore, these modes may capture the eddy activity rather than linear wave adjustment, given the nonlinear nature of the circulation.

For low-frequency variability, the first EOF mode dominates the evolution of the 500-day low-pass flow and accounts for 41% of the total variance (the second mode only contributes 9%). It describes the evolution along the KE axis with a decadal period (Fig. 6), similar to previous model studies (Dewar 2003; Berloff et al. 2007a) and observations (Taguchi et al. 2007). To understand the physics of this mode, we define two indexes for the KE: the KE position index, which is measured by the latitudinal position of the boundary between the subtropical and subpolar gyres averaged zonally within $900 < x < 2900$ km (black curve in Fig. 6b), and KE intensity index, which is defined by the zonally averaged maximum zonal velocity of KE within $900 < x < 2900$ km (black curve in Fig. 6c). It is found that the PC of this mode correlates well with both indexes with correlation coefficients over 0.7 on the 95% confidence level (hereafter all the correlations are significant at the 95% confidence level), implying that the low-frequency variability is characterized by variations of the latitudinal position and intensity of the KE jet. The high correlation also indicates that the KE jet tends to be shifted northward when it is stronger, resembling the model study (Berloff et al. 2007a) and observations (Qiu et al. 2016). Similar conclusions can be obtained for the CL case, indicating that the presence of the SCS does not change the domain patterns and frequencies of oceanic variability in the North Pacific Ocean. In addition, the role of the SCS in regulating the variability of bottom-layer circulation is also explored. In the presence of the SCS, eddy activity is weaker but the low-frequency variability becomes stronger, which is similar to the upper layer (not shown). Thus, we merely focus on the role of the SCS in regulating the upper-layer Pacific circulation hereinafter.

In summary, we find that, in presence of the SCS, both the mean state and eddy activity of the double-gyre circulation is weaker, but the low-frequency variability becomes stronger. In the next section, we will explore the underlying mechanisms.

4. Mechanisms

a. Mean state and eddy activity

In this subsection, we first examine the role of the SCS in influencing the mean circulation and eddy activity of the double-gyre system by exploring the PV dynamics. Here, the streamfunction and PV are decomposed into their time-mean and anomaly state as $\psi_1 = \Psi_1 + \psi_1'$ and $q_1 = Q_1 + q_1'$. Substituting this decomposition into Eq. (1a), integrating it in the entire subtropical gyre, and taking the time average, we obtain the time-mean PV balance equation for the upper-layer subtropical gyre circulation:

$$-\iint_\Omega J(\Psi_1, Q_1)\, dS - \iint_\Omega \overline{J(\psi_1', q_1')}\, dS + \iint_\Omega \frac{f_0}{H_1} W\, dS + \iint_\Omega A_H \nabla^4 \Psi_1\, dS = 0. \tag{10}$$

TABLE 1. Area-integrated PV balances ($10^{-4}\,m^2\,s^{-2}$) for the mean state, state A, and state B in the upper-layer subtropical gyre for the OL case. DSCS is included in the lateral diffusion.

State	Intergyre PV advection	Wind PV input	Lateral diffusion	Total	DSCS
A	−905	−169	+252	−822	−67
B	+118	+64	−67	+115	+113
Mean	3494	−25 725	22 231	0	4059

TABLE 2. Area-integrated PV balances ($10^{-4}\,m^2\,s^{-2}$) for the mean state, state A, and state B in the upper-layer subtropical gyre for the CL case. DSCS is included in the lateral diffusion.

State	Intergyre PV advection	Wind PV input	Lateral diffusion	Total	DSCS
A	−384	−132	+149	−367	+2
B	+27	+212	−41	+198	−11
Mean	4126	−25 621	21 495	0	2515

The overbar in the equation indicates the time average, and Ω is the domain of the time-mean subtropical gyre. The intergyre boundary is defined as the time-mean zero dynamical streamfunction line separating two gyres. Physically, Eq. (10) indicates that PV balance in the subtropical gyre is maintained by the advection of PV by the mean flow and eddies, the wind forcing, and the lateral dissipation. In this equation, there are minus signs before the PV advection terms and thus they represent PV advection into the domain. According to the Gauss formula and no normal flow boundary condition, the areal integration of Jacobian terms equals to the intergyre PV advection $-\int_{\partial\Omega} Q_1 U_{1n}\,dl - \int_{\partial\Omega} \overline{q_1' u_{1n}'}\,dl$. Here, U_{1n} and u_{1n}' are respectively the outward normal mean and anomaly velocity at the boundary of subtropical gyre $\partial\Omega$, and dl is the elementary length. Note that intergyre PV advection caused by mean flow $-\int_{\partial\Omega} Q_1 U_{1n}\,dl$ is zero here because the time-mean velocity is parallel to the isoline of the mean streamfunction, that is, $U_{1n} = 0$. Similarly, the lateral PV dissipation can be transformed into the diffusive flux of vorticity at the solid and intergyre boundaries.

The bottom rows of Tables 1 and 2 summarize the time-mean PV balance in the upper-layer subtropical gyre for two cases. Overall, the PV input by the wind is primarily removed by the lateral dissipation, which accounts for around 85%. The role of SCS [dissipation in the SCS (DSCS)] in the PV balance is defined as the integrated lateral dissipation within the SCS in the OL case and as the integrated dissipation along the western boundary within the latitudinal span of the Luzon Strait ($500 < y < 800$ km) in the CL case. The contribution of the SCS to the PV balance in the CL is $2515 \times 10^{-4}\,m^2\,s^{-2}$ but increases to $4059 \times 10^{-4}\,m^2\,s^{-2}$ (16% of the total wind PV input to the subtropical gyre) in the OL, indicating a much more effective dissipation in the presence of the SCS. This enhanced dissipation explains the weaker mean flow in the presence of the SCS.

To understand the mechanisms in terms of energy, we calculate energy budget following Berloff and Meacham (1998) and Berloff and McWilliams (1999a):

$$\begin{cases} \nabla\cdot\mathbf{M} - \overline{P} - \overline{R} + F + D_H = 0, \\ \dfrac{\partial e}{\partial t} = \nabla\cdot\mathbf{m} + P + R + d_H. \end{cases} \tag{11}$$

The detailed derivation and formulas of terms are given in appendix A. Physically, Eq. (11) shows that the total energy balance (including both upper and lower layers) of the time-mean circulation is maintained by wind energy input F, horizontal flux $\mathbf{M}$, interactions with perturbations P and R, and dissipation D_H, while that of perturbations is maintained by interactions with time-mean flow P and R, horizontal flux $\mathbf{m}$, and dissipation d_H. Here, P is energy transfer from mean to perturbation by Reynolds stress, and R is the same but by interfacial form stress. It is worth noting that all terms in Eq. (8) are surface intensified, and all perturbations are dominated by the high-frequency components. In OL, energy that dissipated in the SCS is $0.9 \times 10^5\,m^4\,s^{-3}$ (7% of the wind input energy), which is 50% larger than lateral dissipation along the western boundary within the latitudinal span of the Luzon Strait in CL (Fig. 7). This further evidences the result from PV analysis that presence of the SCS increases the energy dissipation efficiency of the Pacific circulation.

In addition to the energy that transferred into the SCS, another notable feature is that the basin-integrated value of P becomes significantly smaller in the OL case than in CL (by 25%), corresponding to a weaker eddy energy source in the presence of the SCS. Figure 8a shows the spatial distribution of P in the OL case. Note that only in the KE regions does the perturbation–mean flow interaction appear prominent, so we merely concentrate on this area. It is found that the largest value of P is concentrated at the origin of KE, where the Kuroshio leaves the western boundary. According to previous studies, it is suggested that eddies are generated at the upstream region of KE and carried eastward by the KE jet. During the eastward movement, they continuously extract kinetic energy from the KE and grow to its maximum at the exit region (Berloff et al. 2007b; Waterman and Jayne 2011; Sun et al. 2013). The reduction of P in the OL case is obvious along the KE jet (Fig. 8b), indicating a weaker barotropic instability. This

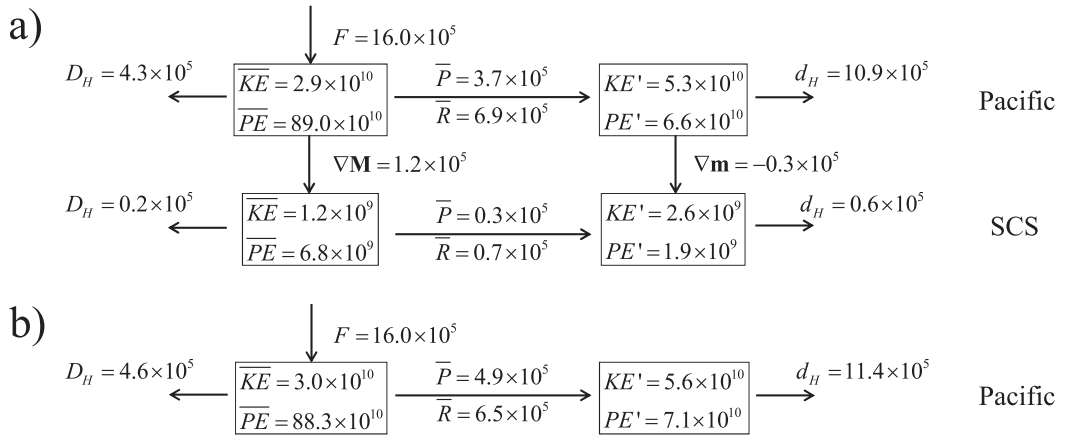

FIG. 7. Schematic of time-mean, area-integrated energy budget analysis for (a) OL and (b) CL. The units are $m^4 s^{-2}$ for KE and PE and $m^4 s^{-3}$ for energy conversion terms.

is likely related to the weaker horizontal shear due to the weaker upstream KE in the OL case. Compared to P, the difference of R between two cases is relatively smaller, indicating that the presence of SCS does not change the baroclinic instability of Pacific circulation significantly.

In short, the weakening of mean circulation in the OL case can be attributed to the intensified dissipation induced by the SCS, which significantly weakens the Kuroshio and upstream KE jet. Consequently, the horizontal shear of the KE gets weaker and the mean flow releases less energy to mesoscale eddies. Because of the reduction of the energy source, eddy activity in OL is weaker.

b. *Low-frequency variability*

In the above discussions, we have talked about the reason for the weaker mean flow and high-frequency variability in OL. In this subsection, we explore the mechanisms that lead to the enhanced low-frequency variability. According to section 3b, low-frequency variability of the North Pacific circulation is characterized by the meridional shift and intensity change of the KE jet, and the KE jet tends to move northward when it gets intensified. Therefore, we will focus on the KE position index in the following discussion. We recognize two states based on the normalized KE position index: state A for the index larger than 1 and state B for the index smaller than −1. State-mean PV balance is calculated for each state shown in Table 1. In both cases, state A is characterized by a negative PV tendency due to anomalous negative wind PV input and reduced intergyre PV advection related to the mean state. On the contrary, boundary dissipation is enhanced due to the increase of both the intensity and meridional length of Kuroshio. The reduced intergyre PV advection indicates that the fully developed oceanic jet acts as a barrier to PV transport associated with the strong relative vorticity gradient across the jet (Berloff et al. 2007a). Different from state A, all terms in state B present different behaviors with a weaker PV input, an intensified intergyre

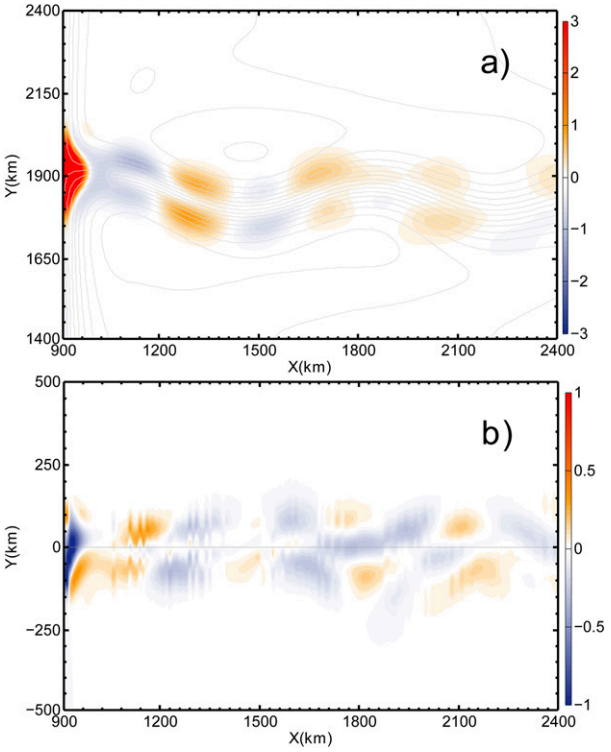

FIG. 8. (a) Spatial distributions of barotropic conversion rate P derived from OL case ($10^{-7} m^2 s^{-3}$). Gray lines are time-mean upper-layer streamfunction. (b) Differences of P between the two cases (OL minus CL). Ordinate indicates the meridional distance from intergyre boundary. Position of intergyre boundary in OL and CL is shown as the black thick line in Figs. 2a and 2b, respectively.

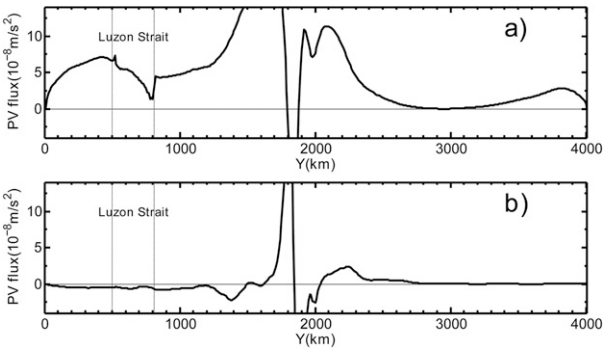

FIG. 9. (a) Zonal-mean meridional PV flux ($10^{-8}\,\mathrm{m\,s^{-2}}$) in OL case and (b) meridional PV flux differences ($10^{-8}\,\mathrm{m\,s^{-2}}$) between the two states (state A minus mean state). Values smaller (greater) than −5 (15) $\times 10^{-8}\,\mathrm{m\,s^{-2}}$ are not shown.

advection, and reduced boundary dissipation. In the OL case, the sign of the DSCS anomaly is always consistent with that of the PV tendency anomaly (last two columns in the Table 1a), implying that the presence of the SCS enhances the low-frequency evolution of the North Pacific circulation. Next, we will further confirm this argument by exploring the low-frequency evolution processes derived for the OL case in detail.

Based on previous sections, the presence of the SCS weakens the downstream Kuroshio and upstream KE (Fig. 3). Correlation analysis shows that the evolution of the KE position/intensity lags the change of DSCS about 100 days. In addition, the evolution of the Kuroshio and KE may react upon DSCS as well. The enhanced KE reduces the intergyre PV advection and lead to the accumulation of negative PV on the southern side of KE. On one hand, this process favors the maintenance of KE by sharpening the PV gradient across the strong jet (Berloff et al. 2007a). On the other hand, the reduced intergyre PV exchange suppresses the positive PV source for the subtropical gyre and results in a weaker zonal-integrated meridional PV flux in the North Pacific. Here, the PV flux is defined as

$$q_1\mathbf{v}_1 = q_1(u_1, v_1). \tag{12}$$

Figure 9a shows the zonal-mean meridional PV flux of the mean state, which is characterized by positive values in the subtropical gyre and well-defined maxima around KE. Compared to that in the mean state, meridional PV flux in state A is significantly reduced within the area $y < 1500$ km (Fig. 9b). Zonal-mean meridional PV flux in the band $500 < y < 800$ km lags the KE position/intensity index about 680 days with correlation around −0.4 (the correlation is computed based on 500-day low-pass time series). Comparison of the PV flux map between state A and mean state (not shown) indicates this change is mainly caused by the flux in the inner ocean, which may be associated with the horizontal advection. We prove this by regressing the streamfunction anomaly onto the KE position index along the time-mean, 20-Sv streamline between point M ($x = 1670$ km, $y = 650$ km) and point N ($x = 3070$ km, $y = 1650$ km; Fig. 10a). In response to the changes in the vicinity of KE, anomalies begin to appear around point N and then propagate southwestward along the streamline. According to Fig. 10b, it takes the streamfunction anomaly about 600 days to arrive at point M. The speed of the streamfunction anomaly is about $4.5\,\mathrm{cm\,s^{-1}}$, in agreement with the time-mean velocity along the streamline. In the ocean, evolution of the streamfunction would change the flow field and thus regulate the PV flux. This can be indicated from Fig. 10c, in which the streamfunction anomaly tracks well with the meridional PV flux with correlation exceeding 0.6. In addition to the 20-Sv streamline, the same examination

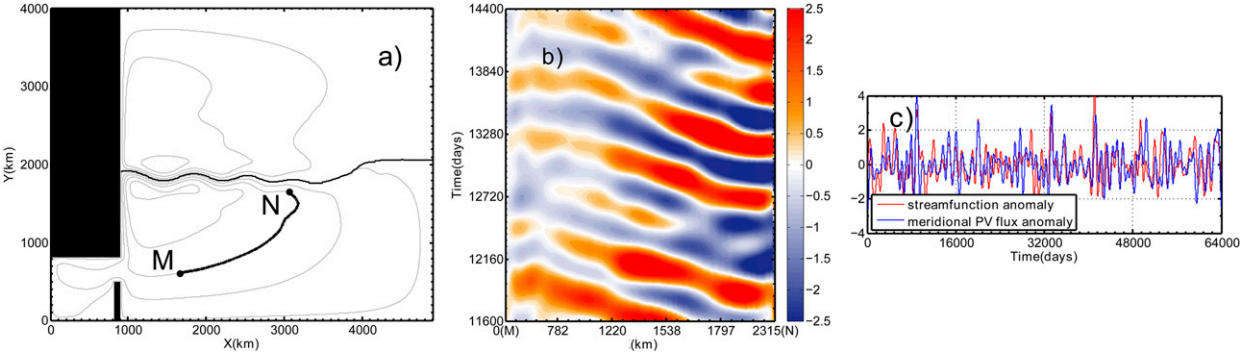

FIG. 10. (a) The time-mean upper-layer streamfunction (Sv; gray). The black line between M ($x = 1670$ km, $y = 650$ km) and N ($x = 3070$ km, $y = 1650$ km) is used to trace the streamfunction anomaly. (b) Streamfunction anomaly regressed onto the KE position index along the streamfunction line shown in (a) between 11 600 and 14 400 model days. (c) Normalized streamfunction anomaly and meridional PV flux anomaly at point M. Here, the analysis is based on the 500-day low-pass data.

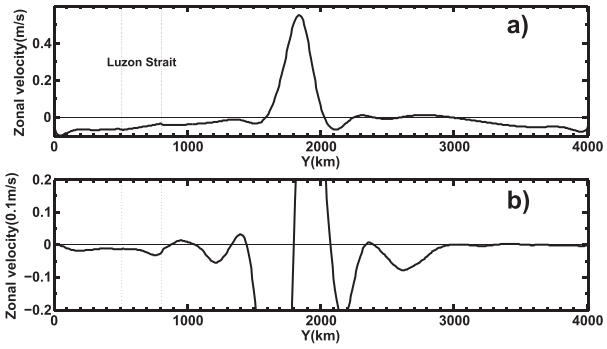

FIG. 11. (a) Zonal-mean zonal velocity u ($\mathrm{m\,s^{-1}}$) in OL case and (b) zonal velocity differences ($0.1\,\mathrm{m\,s^{-1}}$) between the two states (state A minus mean state). In b), values smaller (greater) than -0.02 (0.02) $\mathrm{m\,s^{-1}}$ are not shown.

is also applied to streamlines successively from 10 to 21 Sv, and similar results are found, further guaranteeing our conclusion.

Change of the meridional PV flux results in the evolution of zonal flow, which can be inferred from the eddy rectification equation (appendix B):

$$\frac{\partial \overline{u_1}^x}{\partial t} = \lambda \overline{q_1 v_1}^x, \tag{13}$$

where $^{-x}$ represents the zonal mean. The parameter λ is a weight coefficient, which describes the proportion of relative PV in the absolute PV. It can be inferred from the derivation that evolution of $\overline{u_1}^x$ is actually related to Reynolds effects [Eq. (B6)], which are associated with the relative PV component. Physically, this process is driven by the meridional mixing and partial homogenization of PV (Berloff et al. 2007b). According to Eq. (13), negative meridional PV flux anomaly will lead to westward acceleration. This can be further supported by the comparison of $\overline{u_1}^x$ between state A and the mean state (Fig. 11). Compared to the mean state, zonal velocity in state A is intensified within the area $y < 1500$ km. Coinstantaneous correlation between the meridional PV flux in the region $x > 910$ km, $500 < y < 800$ km and mean zonal speed along the line $x = 1000$ km, $500 < y < 800$ km approaches 0.5. Evolution of $\overline{u_1}^x$ regulates the zonal PV flux in that latitude and results in convergence of negative PV on the eastern side of the Kuroshio (Fig. 12a; time series of normalized zonal PV flux across the line $x = 1000$ km, $500 < y < 800$ km is same as that of zonal speed). As a result, the Kuroshio in the vicinity of the Luzon Strait is enhanced (Fig. 12b), which favors the anticyclonic Kuroshio loop (Fig. 2) retreating from the SCS because of its larger inertia (Sheremet 2001; Hu et al. 2015). At last, the DSCS is reduced (Fig. 12c). Correlation between DSCS and the mean zonal speed along the

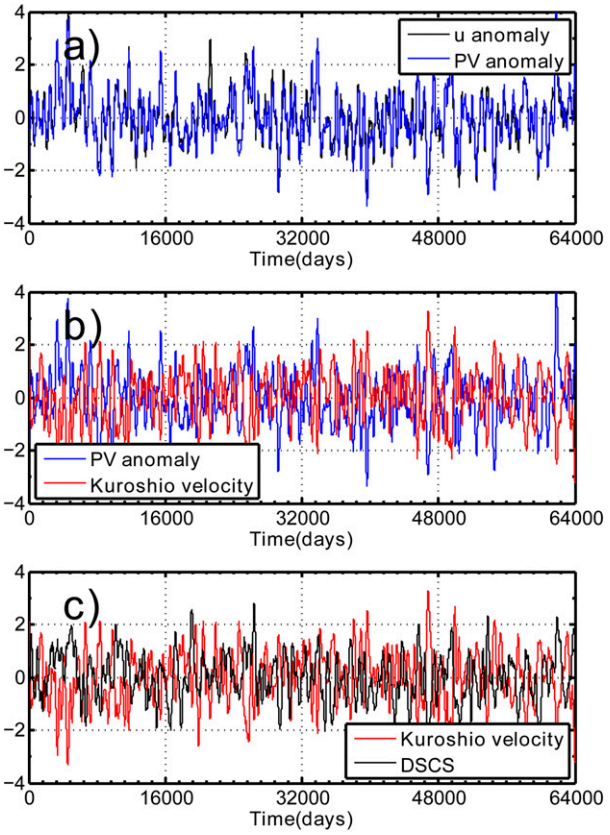

FIG. 12. Normalized mean zonal velocity anomaly along the line $x = 1000$ km, $500 < y < 800$ km [black line in (a)], normalized area-mean PV within $910 < x < 1000$ km, $500 < y < 800$ km [blue lines in (a) and (b)], normalized Kuroshio velocity within $500 < y < 800$ km [red lines in (b) and (c)], and normalized DSCS [black line in (c)]. Correlations between curves in (a), (b), and (c) are 0.94, -0.88, and -0.63, respectively.

line $x = 1000$ km, $500 < y < 800$ km exceeds 0.5 when DSCS lags about 100 days. Overall, north-shifted KE results in a weaker DSCS.

Based on the above findings, we conclude the physical processes underlying the promoting role of the SCS for low-frequency variability in the double-gyre system (Fig. 13). When the KE shifts to the north, its transport tends to be larger compared to the mean state. Thus, the intergyre PV exchange is reduced and negative PV accumulates on the southern side of KE. These two processes suppress the northward meridional PV flux in the subtropical gyre, which induces a westward zonal flow anomaly and then results in a stronger Kuroshio around the Luzon Strait. Because of its larger inertia, the Kuroshio tends to retreat from the SCS and leads to a smaller DSCS, which enhances the intensity of downstream Kuroshio in the OL case. Finally, the intensified Kuroshio favors the north shifting and intensification of KE. The period of this positive feedback is less than 3 years, which

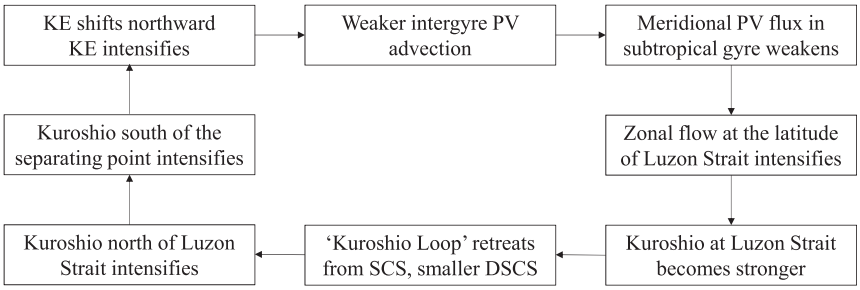

FIG. 13. Schematic diagrams of the positive feedback induced by the presence of SCS.

is much smaller compared to that of the low-frequency evolution in the Pacific Ocean (Fig. 6). The process associated with south-shifted KE is similar. However, these positive feedback processes will be terminated by the low-frequency evolution of the double-gyre system. With the north shifting and enhancing of the KE jet, negative PV accumulates continually in the subtropical gyre because of the increased wind input and reduced intergyre exchange. The accumulated PV continually increases the recirculation strength. On one hand, the intensified recirculation pulls the KE southward and shrinks the subtropical gyre, which reduces the wind PV input (Chang et al. 2001; Berloff et al. 2007a); on the other hand, it increases the dissipations along western boundary due to the enhanced horizontal velocity shear (Dijkstra and Ghil 2005; Berloff et al. 2007a). As a result, the double-gyre circulation shifts to state B.

In addition, the detailed evolutional process in the CL case is also examined (figure not shown). The positive feedback in OL is not established because DSCS changes consistently with the speed of the Kuroshio within $450 < y < 800$ km (correlation is 0.6). To further support this conclusion, we perform CL with the value of A_H along the western boundary within the latitudinal range of the Luzon Strait increasing to $2500\,\mathrm{m^2\,s^{-1}}$. In this case, both the time-mean subtropical gyre and eddy activity are weaker compared to their counterparts in the CL case (Figs. 14a,b) because the Kuroshio is weaker, consistent with the above conclusion. However, the low-frequency variability of the Pacific Ocean derived from this case is found to be weaker than the CL case (Fig. 14c). Moreover, PV budget analysis is also examined for different states of the KE jet during the low-frequency evaluation in Table 3. Sign of DSCS anomaly is found to be always contrary to the sign of PV tendency anomaly, which is indicative of the damping role of the DSCS. Correlation between DSCS and the mean Kuroshio velocity within $x = 910$ km, $450 < y < 800$ km exceeds 0.7, further demonstrating that the positive feedback cannot be established without the SCS.

To summarize this subsection, the low-frequency variability of the North Pacific circulation is characterized by meridional shift and intensity change of the KE jet in both OL and CL cases, but the variability is stronger in OL because of the positive feedback induced by the presence of SCS.

c. *Sensitivity study*

We first conduct the parameter sensitivity runs by varying the wind forcing. Figures 15a and 15b show the mean upper-layer circulations driven by winds of $0.6W$ and $1.4W$ [where W is defined in Eq. (3)]. Both of these

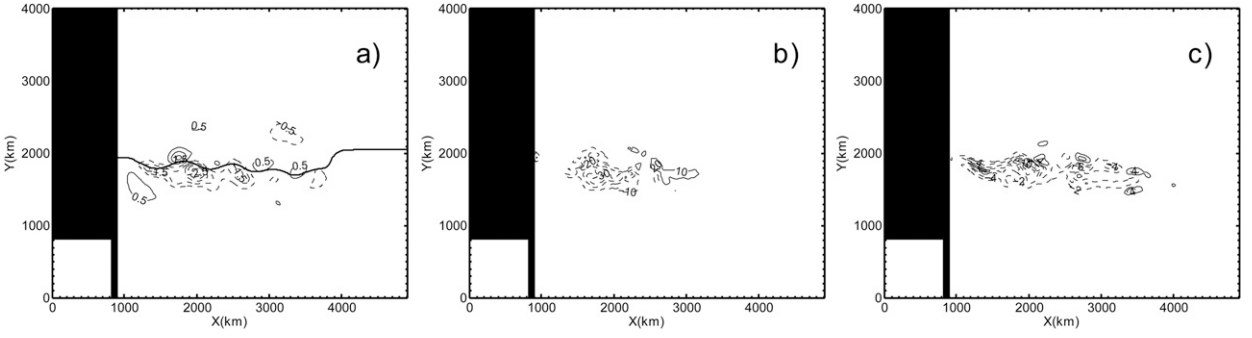

FIG. 14. Differences of (a) upper-layer streamfunction (Sv; CI = 0.5 Sv), (b) $0.5\mathbf{U}'^2_{\mathrm{high}}$ ($0.001\,\mathrm{m^2\,s^{-2}}$; CI = $0.01\,\mathrm{m^2\,s^{-2}}$), and (c) $0.5\mathbf{U}'^2_{\mathrm{low}}$ between the two cases (CI = $0.002\,\mathrm{m^2\,s^{-2}}$; CL with $A_H = 2500\,\mathrm{m^2\,s^{-2}}$ along the Luzon Strait minus CL).

TABLE 3. Area-integrated PV balances ($10^{-4}\,m^2\,s^{-2}$) for the mean state, state A, and state B in the upper-layer subtropical gyre in the case with closed Luzon Strait and $A_H = 2500\,m^2\,s^{-1}$ within the latitudinal range of the Luzon Strait. DSCS is included in the lateral diffusion.

State	Intergyre PV advection	Wind PV input	Lateral diffusion	Total	DSCS
A	−254	−132	+28	−358	+8
B	+5	+191	−130	+67	−25
Mean	3915	−25 624	21 709	0	3196

solutions depict double-gyre patterns. Transport of the Loop Current in the SCS of the 0.6*W* run is 12 Sv, which accounts for 50% of the transport of the subtropical gyre (25 Sv), while that derived from the 1.4*W* run is only 36% (18/50 Sv). Thus, the Kuroshio intrusion in the 0.6*W* run is more obvious compared to the 1.4*W* run. According to the PV budget, the relative contribution of DSCS in the PV balance of the North Pacific is larger in the 0.6*W* run (not shown), indicating a larger role of the SCS in weakening the Kuroshio in the 0.6*W* run. For low-frequency variability, the ratio between variability of DSCS and time-mean PV input into the subtropical gyre is also larger in the 0.6*W* run, suggesting a larger, promoting role of the SCS in regulating the low-frequency evolution of the double-gyre system. Sensitivity experiments for eddy viscosity A_H are shown in Figs. 15c and 15d, in which the behavior of the circulation seems to be insensitive to the eddy viscosity in the range of 100 and 200 $m^2\,s^{-1}$. It is also confirmed through PV budget that the contribution of the SCS in weakening the Kuroshio and regulating the Pacific low frequency is much larger in the higher A_H case (not shown). Based on the results of sensitivity to wind forcing and A_H, we could expect a smaller contribution of the SCS in the circulation system within stronger, nonlinear flow regimes. In addition, the low-frequency variability of double-gyre circulation tends to depict a shorter period in a stronger, nonlinear regime (i.e., smaller A_H or larger wind forcing), in agreement with previous study (Berloff et al. 2007a).

Sensitivities associated with the Luzon Strait are also explored by varying its position and width. By successively varying the width of the strait from 100 to 500 km, it is found that a narrow strait prevents the Kuroshio from intruding into the SCS (Fig. 15e), while the Kuroshio intrudes into the SCS significantly as the strait becomes sufficiently wide (Fig. 15f). These results are consistent with the theoretical analysis by Sheremet (2001), which predicts a strong Kuroshio intrusion when the strait is wider. The contribution of the SCS in influencing the Pacific Ocean is found to increase with the width of the Luzon Strait. We also conduct some runs by moving the Luzon Strait 200 km southward (Fig. 14g) and northward (Fig. 14h), and results show that the influence of the SCS increases with the northward movement of the strait.

Differing from other parameters, the model solutions are found to be sensitive to the boundary condition (Figs. 15i–l). When α is close to the reference value ($\alpha = 0.025,\ 0.1\,km^{-1}$; Figs. 15k,l), the mean fields are characterized by the double-gyre patterns with similar transports to the reference solution. However, the feature of variability is not generic as the partial-slip parameter approaches its limits. For $\alpha = 0$ (free-slip boundary; Fig. 15j), the mean field depicts a reduced subtropical gyre with a significant Kuroshio intrusion. In accordance with this, much stronger variability of the KE induced by much larger P and R is present (not shown). In another case, as α approaches infinity (no-slip boundary; Fig. 15i), KE variability is largely suppressed due to the extreme viscous stress on the boundary.

According to the observations, the KE is located significantly to the south of the zero Ekman pumping line and is clearly separated with the Oyashio Extension (early separation; Yasuda 2003; Nakano et al. 2008). To approach this fact, we perform OL and CL cases with the no-slip condition, $A_H = 100\,m^2\,s^{-1}$, and wind forcing:

$$W_1 = \begin{cases} -1.5\times10^{-6}\times\left[\sin\left(\dfrac{2\pi}{L_y}y\right)+0.1\sin\left(\dfrac{\pi}{L_y}y\right)\right] & W_1 \geq 0, \\ -2.5\times10^{-6}\times\left[\sin\left(\dfrac{2\pi}{L_y}y\right)+0.1\sin\left(\dfrac{\pi}{L_y}y\right)\right] & W_1 < 0. \end{cases} \tag{14}$$

Here, the wind forcing is set to be stronger in the subtropical gyre and more asymmetric than the standard run. Figure 16a shows the mean upper-layer streamfunction derived from OL. In these two cases, the KE and Oyashio Extension are significantly separated, and the northern recirculation gyre is only associated with the KE. The total transport of the recirculation south of KE is stronger (110 Sv), and the meridional distance between the Kuroshio separating point and zero Ekman pumping line approaches 600 km, closer to the observations than the

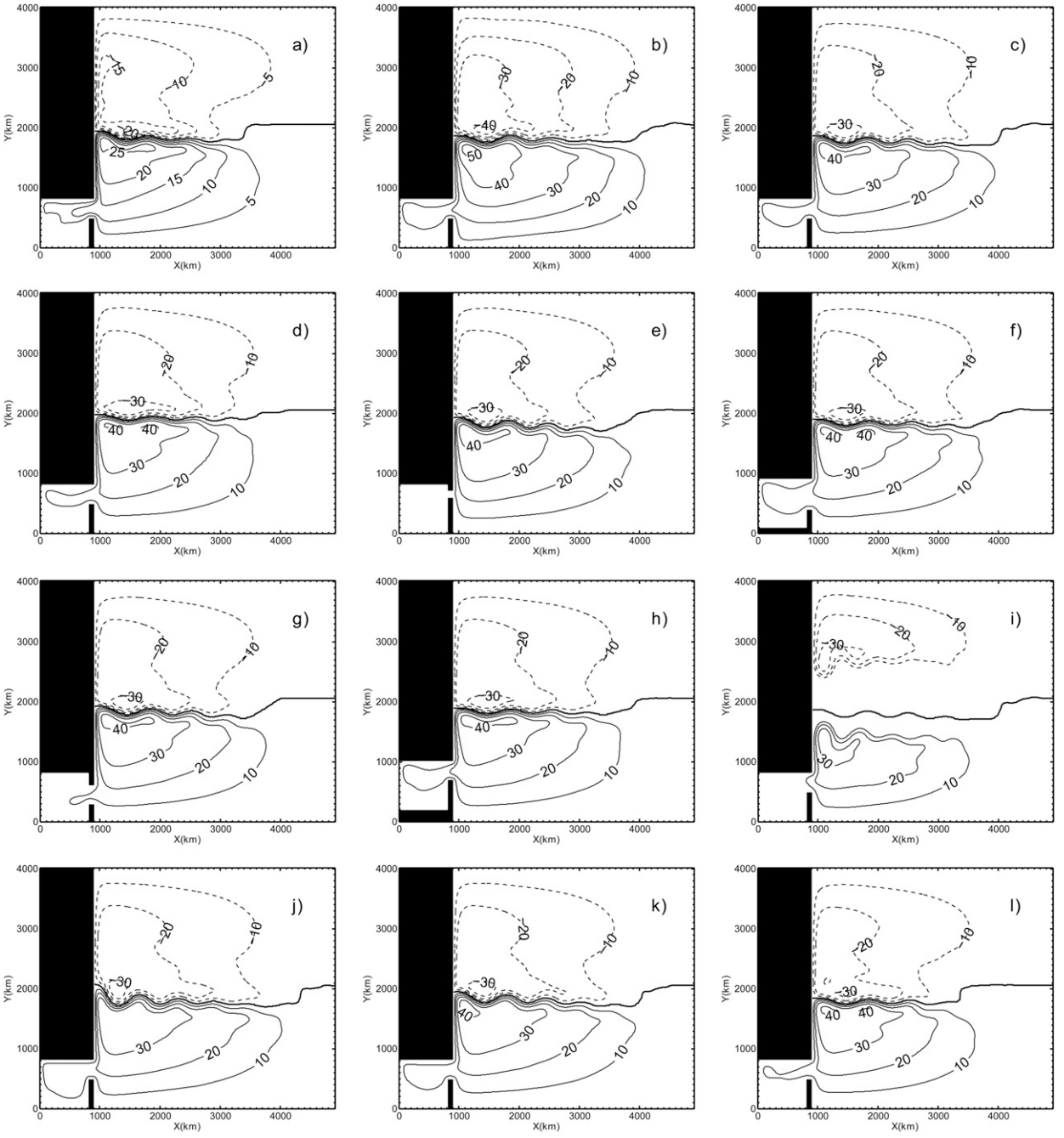

FIG. 15. Time-mean upper-layer streamfunctions for varying parameters (Sv; CI = 10 Sv). (a) 0.6W forcing, (b) 1.4W forcing, (c) A_H = 100 m^2 s^{-1}, (d) A_H = 200 m^2 s^{-1}, (e) l_s = 100 km, (f) l_s = 500 km, (g) strait moves southward 200 km, (h) strait moves northward 200 km, (i) nonslip condition, (j) free-slip condition, (k) α = 0.025 km^{-1}, and (l) α = 0.1 km^{-1}. All the runs are conducted with other parameters being fixed.

reference solution. With the presence of SCS, the time-mean subtropical gyre and eddy activity along the KE are significantly weaker (Figs. 16d,e), consistent with reference solutions. Moreover, the presence of SCS is found to promote the low-frequency evolution of the Pacific circulation in the KE region (Fig. 16f). Overall, the result in the paper does not change much if the Kuroshio separates from the coast earlier.

5. Summary

Using a two-layer QG model, the role of the SCS in regulating the double-gyre system is investigated in this

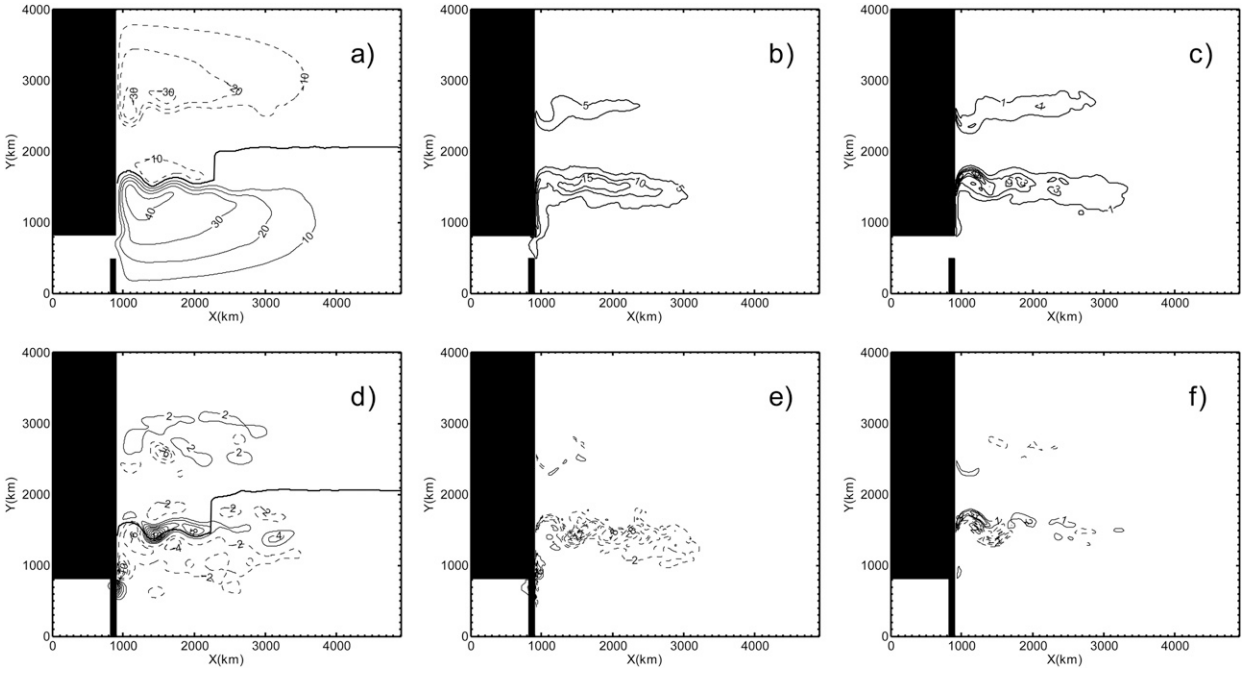

FIG. 16. (a) Mean upper-layer streamfunctions in OL (Sv; CI = 10 Sv), (b) $0.5\mathbf{U}^2_{\text{high}}$ ($0.01\ \text{m}^2\ \text{s}^{-2}$; CI = $0.05\ \text{m}^2\ \text{s}^{-2}$), and (c) $0.5\mathbf{U}^2_{\text{low}}$ (CI = $0.02\ \text{m}^2\ \text{s}^{-2}$) under no-slip condition, wind forcing W_1, and smaller A_H. Differences of (d) upper-layer streamfunction (CI = 2 Sv), (e) $0.5\mathbf{U}^2_{\text{high}}$ (CI = $0.02\ \text{m}^2\ \text{s}^{-2}$), and (f) $0.5\mathbf{U}^2_{\text{low}}$ (CI = $0.01\ \text{m}^2\ \text{s}^{-2}$) between the two cases (OL minus CL).

study. The major results of the present study are summarized as follows:

1) The SCS acts as a sink of PV and energy in the Pacific–SCS system, accounting for 16% of the PV input by wind into the subtropical gyre and 7% of the energy input by wind into the double-gyre circulation. Correspondingly, both the Kuroshio and the upstream KE are weakened in the OL case compared with the CL case. The weakening of the Kuroshio and KE further affects the barotropic instability, leading to a weaker eddy activity in the North Pacific Ocean.
2) The SCS is found to promote the low-frequency evolution of the Pacific circulation in the KE region (meridional shift and intensity change of KE jet). This is mainly caused by a positive feedback process associated with the negative correlation between the inertia of the Kuroshio and the Kuroshio intrusion at the Luzon Strait that the presence of the SCS provides.

It should be noted that more studies are needed to clarify the role of continental slope and coastline orientation of the North Pacific Ocean in influencing the results in this study, given their roles in regulating the western boundary currents (Hughes and de Cuevas 2001). The details of the topography around the Luzon Strait may affect the Kuroshio intrusion in the SCS (Lu and Liu 2013), which is not considered in the current study. Furthermore, the processes that cannot be simulated by idealized the QG model, such as the mixing zone between KE and Oyashio Extension (Yasuda 2003), the outcropping of the thermocline, and Kelvin waves should be investigated in more details in the future with high-resolution ocean general circulation models.

Acknowledgments. This research is supported by National Natural Science Foundation of China Project (41490640, 41490643, 41622602, and U1606402), Funds for Creative Research Groups of China (41521091), National Key Scientific Instrument and Equipment Development Projects of China (41527901), WenHai Project of Shandong Province (2016WH03ZR), Special Fund for the Strategic Priority Research Program of the Chinese Academy of Sciences (XDA11010101), Global Change and Air-Sea Interaction Project (GASI-03-01-01-05), and National Science Foundation of the United States (OCE-1357078). The authors thank Prof. Jiayang Yang and Prof. Bo Qiu for helpful advice. Comments from two anonymous reviewers are greatly appreciated.

APPENDIX A

Energetics

We decompose the streamfunction into the mean and anomaly state as $\psi_1 = \Psi_1 + \psi_1'$ and $\psi_2 = \Psi_2 + \psi_2'$.

Following Berloff and McWilliams (1999a), the energy density of the mean state is defined as

$$E(x,y)=\sum_{i=1,2}\frac{H_i}{H}\frac{|\nabla\Psi_i|^2}{2}+\frac{f_0^2}{2g'H}(\Psi_1-\Psi_2)^2, \quad \text{(A1)}$$

and the perturbation energy density is

$$e(x,y,t)=\sum_{i=1,2}\frac{H_i}{H}\frac{|\nabla\psi_i'|^2}{2}+\frac{f_0^2}{2g'H}(\psi_1'-\psi_2')^2. \quad \text{(A2)}$$

Here, $|\ |$ means modulus for vectors, and $H=H_1+H_2$. By multiplying Eq. (1a) by $\Psi_1\times H_1/H$ and Eq. (1b) by $\Psi_2\times H_2/H$ and then adding the two resulting equations together and taking a time average, we get the energy equation of the mean state:

$$\frac{\partial E}{\partial t}=\nabla\cdot\mathbf{M}-\overline{P}-\overline{R}+F+D_H=0. \quad \text{(A3)}$$

In this equation, the bar denotes the time mean. The formula of the time-mean energy flux $\mathbf{M}$ is

$$\begin{aligned}\mathbf{M}=&\left\{\frac{H_1}{H}\frac{\Psi_1^2}{2}\left(\nabla^2\frac{\partial\Psi_1}{\partial y}+\frac{f_0^2}{g'H_1}\frac{\partial\Psi_2}{\partial y}\right)+\frac{H_2}{H}\frac{\Psi_2^2}{2}\left(\nabla^2\frac{\partial\Psi_2}{\partial y}+\frac{f_0^2}{g'H_2}\frac{\partial\Psi_1}{\partial y}\right)\right.\\
&+\sum_{i=1,2}\frac{H_i}{H}\left[-\Psi_i\overline{\frac{\partial\psi_i'}{\partial y}\nabla^2\psi_i'}+\frac{\partial\Psi_i}{\partial x}\overline{\frac{\partial\psi_i'}{\partial x}\frac{\partial\psi_i'}{\partial y}}-\frac{\partial\Psi_i}{2\partial y}\overline{\left(\frac{\partial\psi_i'}{\partial x}\right)^2-\left(\frac{\partial\psi_i'}{\partial y}\right)^2}\right]\\
&\left.+\frac{f_0^2}{2g'H}(\Psi_1-\Psi_2)\overline{(\psi_1'-\psi_2')\frac{\partial(\psi_1'+\psi_2')}{\partial y}}+\sum_{i=1,2}\beta\frac{H_i}{H}\frac{\Psi_i^2}{2}\right\}\mathbf{i}\\
&-\left\{\frac{H_1}{H}\frac{\Psi_1^2}{2}\left(\nabla^2\frac{\partial\Psi_1}{\partial x}+\frac{f_0^2}{g'H_1}\frac{\partial\Psi_2}{\partial x}\right)+\frac{H_2}{H}\frac{\Psi_2^2}{2}\left(\nabla^2\frac{\partial\Psi_2}{\partial x}+\frac{f_0^2}{g'H_2}\frac{\partial\Psi_1}{\partial x}\right)\right.\\
&-\sum_{i=1,2}\frac{H_i}{H}\left[-\Psi_i\overline{\frac{\partial\psi_i'}{\partial x}\nabla^2\psi_i'}+\frac{\partial\Psi_i}{\partial y}\overline{\frac{\partial\psi_i'}{\partial x}\frac{\partial\psi_i'}{\partial y}}-\frac{\partial\Psi_i}{2\partial x}\overline{\left(\frac{\partial\psi_i'}{\partial x}\right)^2-\left(\frac{\partial\psi_i'}{\partial y}\right)^2}\right]\\
&\left.+\frac{f_0^2}{2g'H}(\Psi_1-\Psi_2)\overline{(\psi_1'-\psi_2')\frac{\partial(\psi_1'+\psi_2')}{\partial x}}\right\}\mathbf{j}+A_H\sum_{i=1,2}\frac{H_i}{H}(\nabla^2\Psi_i\nabla\Psi_i-\Psi_i\nabla\nabla^2\Psi_i). \quad \text{(A4)}\end{aligned}$$

The energy exchange terms between the mean state and the perturbations are

$$P=-\sum_{i=1,2}\frac{H_i}{H}\left[\frac{\partial\psi_i'}{\partial x}J\left(\psi_i',\frac{\partial\Psi_i}{\partial x}\right)+\frac{\partial\psi_i'}{\partial y}J\left(\psi_i',\frac{\partial\Psi_i}{\partial y}\right)\right], \quad \text{(A5)}$$

and

$$R=-\frac{f^2}{g'H}(\psi_1'-\psi_2')J(\psi_1'+\psi_2',\Psi_1-\Psi_2). \quad \text{(A6)}$$

Here, P is the energy exchange between the mean state and perturbations due to the work done by horizontal Reynolds stress, and R is the energy exchange due to the work done by isopycnal form stress associated with divergence of the heat flux of the fluctuations. The wind forcing term F and lateral dissipation of mean energy are

$$F=-\frac{f}{H}\Psi_1 W, \quad \text{(A7)}$$

and

$$D_H=-A_H\sum_{i=1,2}\frac{H_I}{H}(\nabla^2\Psi_i)^2. \quad \text{(A8)}$$

Similar to the mean state, the energy equation for perturbation is determined by multiplying Eq. (1a) by $\psi_1'\times H_1/H$ and Eq. (1b) by $\psi_2'\times H_2/H$ and adding the two resulting equations together:

$$\frac{\partial e}{\partial t} = \nabla \cdot \mathbf{m} + P + R + d_H. \tag{A9}$$

The energy flux $\mathbf{m}$ and lateral dissipation of mean energy are

$$\begin{aligned}
\mathbf{m} = & \sum_{i=1,2} \frac{H_i}{H} \psi_i' \nabla \frac{\partial \psi_i'}{\partial t} + \left(\sum_{i=1,2} \frac{H_i}{H} \frac{\psi_i'^2}{2} \nabla^2 \frac{\partial (\Psi_i + \psi_i')}{\partial y} \right. \\
& + \sum_{i=1,2} \frac{H_i}{H} \left\{ -\psi_i' \frac{\partial \Psi_i}{\partial y} \nabla^2 \psi_i' - \frac{\partial \psi_i'}{\partial x} \frac{\partial \psi_i'}{\partial y} \frac{\partial \Psi_i}{\partial x} + \frac{\partial \Psi_i}{2 \partial y} \left[\left(\frac{\partial \psi_i'}{\partial x} \right)^2 - \left(\frac{\partial \psi_i'}{\partial y} \right)^2 \right] \right\} \\
& + \frac{f_0^2}{2 g' H} \left[\psi_1' \frac{\partial (\Psi_2 + \psi_2')}{\partial y} + \psi_2' \frac{\partial (\Psi_1 + \psi_1')}{\partial y} \right] \\
& + \frac{f_0^2}{2 g' H} \left[(\psi_1' + \psi_2')(\psi_1' - \psi_2') \frac{\partial (\Psi_1 - \Psi_2)}{2 \partial y} - \psi_1' \psi_2' \frac{\partial (\Psi_1 + \Psi_2)}{\partial y} \right] + \sum_{i=1,2} \beta \frac{H_i}{H} \frac{\psi_i'^2}{2} \Bigg) \mathbf{i} \\
& - \left(\sum_{i=1,2} \frac{H_i}{H} \frac{\psi_i'^2}{2} \nabla^2 \frac{\partial (\Psi_i + \psi_i')}{\partial x} \right. \\
& + \sum_{i=1,2} \frac{H_i}{H} \left\{ -\psi_i' \frac{\partial \Psi_i}{\partial x} \nabla^2 \psi_i' - \frac{\partial \psi_i'}{\partial x} \frac{\partial \psi_i'}{\partial y} \frac{\partial \Psi_i}{\partial y} + \frac{\partial \Psi_i}{2 \partial x} \left[\left(\frac{\partial \psi_i'}{\partial x} \right)^2 - \left(\frac{\partial \psi_i'}{\partial y} \right)^2 \right] \right\} \\
& + \frac{f_0^2}{2 g' H} \left[\psi_1' \frac{\partial (\Psi_2 + \psi_2')}{\partial x} + \psi_2' \frac{\partial (\Psi_1 + \psi_1')}{\partial x} \right] \\
& + \frac{f_0^2}{2 g' H} \left[(\psi_1' + \psi_2')(\psi_1' - \psi_2') \frac{\partial (\Psi_1 - \Psi_2)}{2 \partial x} - \psi_1' \psi_2' \frac{\partial (\Psi_1 + \Psi_2)}{\partial x} \right] \Bigg) \mathbf{j} \\
& + A_H \sum_{i=1,2} \frac{H_i}{H} (\nabla^2 \psi_i' \nabla \psi_i' - \psi_i' \nabla \nabla^2 \psi_i'),
\end{aligned} \tag{A10}$$

and

$$d_H = -A_H \sum_{i=1,2} \frac{H_I}{H} (\nabla^2 \psi_i')^2. \tag{A11}$$

In this study, we ignore the energy dissipation caused by bottom friction because it is smaller than other terms by at least an order of magnitude.

APPENDIX B

PV Flux and Zonal Flow

As the motion in the bottom layer is much weaker than that in the upper layer, we derive Eq. (13) based on the 1.5-layer original momentum equation. Considering the reduced-gravity equation with weak dissipation:

$$\frac{\partial u}{\partial t} + u \frac{\partial u}{\partial x} + v \frac{\partial u}{\partial y} - f v = -g' \frac{\partial h}{\partial x}. \tag{B1}$$

Here, (u, v) represent horizontal velocity, and h is the upper-layer depth anomaly. This equation is obtained by subtracting the large-scale balance ($-fv = -g'\partial h/\partial x + A_H \partial^2 u/\partial x^2 + \tau/h$) from the momentum equation and ignoring the viscous term for the perturbation. Taking the zonal average of Eq. (B1), we get

$$\frac{\partial \overline{u}^x}{\partial t} + u \overline{\frac{\partial u}{\partial x}}^x + v \overline{\frac{\partial u}{\partial y}}^x - f \overline{v}^x = -g' \overline{\frac{\partial h}{\partial x}}^x. \tag{B2}$$

The notation $\overline{\ }^x$ represents the zonal mean. In a closed basin, we have

$$\overline{v}^x \approx 0, \tag{B3}$$

$$\overline{\frac{\partial h}{\partial x}}^x = \frac{1}{X} \int_{\text{west}}^{\text{east}} \frac{\partial h}{\partial x} dx = \frac{1}{X} \int_{\text{west}}^{\text{east}} dh \approx 0, \tag{B4}$$

and

$$u \overline{\frac{\partial u}{\partial x}}^x = \frac{1}{2} \overline{\frac{\partial u^2}{\partial x}}^x = \frac{1}{2X} \int_{\text{west}}^{\text{east}} \frac{\partial u^2}{\partial x} dx = \frac{1}{2X} \int_{\text{west}}^{\text{east}} du^2 = 0. \tag{B5}$$

Here, X is the distance between western and eastern boundaries. In the low-frequency evolution, Eqs. (B3) and (B4) [$\sim O(10^{-8})\,\mathrm{m\,s^{-2}}$] are smaller than the nonlinear terms [$\sim O(10^{-7})\,\mathrm{m\,s^{-2}}$] by an order of magnitude. Thus,

$$\frac{\partial \overline{u}^x}{\partial t} = -\overline{\frac{\partial u}{\partial y} v}^x . \tag{B6}$$

In the reduced-gravity model, the formula of PV is $[(\partial v/\partial x) - (\partial u/\partial y) - f(h/H_1)]$, where H_1 is the mean thickness of the upper-layer ocean [Eq. (1a)]. In the area of westward return currents, $\partial v/\partial x$ is very small. It is diagnosed that the relative PV changes in accord with the thickness PV. Therefore, the right-hand side of Eq. (B6) can be expressed in terms of PV:

$$\frac{\partial \overline{u}^x}{\partial t} = -\overline{\frac{\partial u}{\partial y} v}^x \triangleq \lambda \overline{q v}^x . \tag{B7}$$

By comparing the area mean absolute value of relative PV and thickness PV in the Pacific Ocean, we get $\lambda = 0.05$. In the QG model, the scale ratio between relative PV and thickness PV is $(1/L^2):[f_0^2/(g' H_1)]$. Substituting the value of λ and we get $L \sim O(190)$ km, which is the length scale of nonlinear eddies (Rhines scale varies from 80 $\sim$ 320 km in our model). Thus, this phenomenon may be caused by eddies.

Quantitatively, the standard deviation of zonal-mean meridional PV flux within $500 < y < 800$ km is $O(10^{-8})\,\mathrm{m\,s^{-2}}$ and λ is $O(0.01)$. Time scale is $O(10^7)$ s. Thus, Eq. (12) speculates the change of zonal-mean u is $O(10^{-3})\,\mathrm{m\,s^{-1}}$, which is comparable to the standard deviation of the zonal-mean u within $500 < y < 800$ km.

REFERENCES

Berloff, P., and S. Meacham, 1998: On the stability of the wind-driven circulation. *J. Mar. Res.*, **56**, 937–993, doi:10.1357/002224098765173437.

——, and J. McWilliams, 1999a: Large-scale, low-frequency variability in wind-driven ocean gyres. *J. Phys. Oceanogr.*, **29**, 1925–1949, doi:10.1175/1520-0485(1999)029<1925:LSLFVI>2.0.CO;2.

——, and ——, 1999b: Quasigeostrophic dynamics of the western boundary current. *J. Phys. Oceanogr.*, **29**, 2607–2634, doi:10.1175/1520-0485(1999)029<2607:QDOTWB>2.0.CO;2.

——, A. Hogg, and W. Dewar, 2007a: The turbulent oscillator: A mechanism of low-frequency variability of the wind-driven ocean gyres. *J. Phys. Oceanogr.*, **37**, 2363–2386, doi:10.1175/JPO3118.1.

——, S. Kravtsov, W. Dewar, and J. McWilliams, 2007b: Ocean eddy dynamics in a coupled ocean–atmosphere model. *J. Phys. Oceanogr.*, **37**, 1103–1121, doi:10.1175/JPO3041.1.

Cessi, P., 1988: A stratified model of the inertial recirculation. *J. Phys. Oceanogr.*, **18**, 662–682, doi:10.1175/1520-0485(1988)018<0662:ASMOTI>2.0.CO;2.

——, and F. Primeau, 2001: Dissipative selection of low-frequency modes in a reduced-gravity basin. *J. Phys. Oceanogr.*, **31**, 127–137, doi:10.1175/1520-0485(2001)031<0127:DSOLFM>2.0.CO;2.

Chang, K., M. Ghil, K. Ide, and C. Lai, 2001: Transition to aperiodic variability in a wind-driven double-gyre circulation model. *J. Phys. Oceanogr.*, **31**, 1260–1286, doi:10.1175/1520-0485(2001)031<1260:TTAVIA>2.0.CO;2.

Chang, Y., C. Wu, and L. Oey, 2009: Bimodal behavior of the seasonal upwelling off the northeastern coast of Taiwan. *J. Geophys. Res.*, **114**, C03027, doi:10.1029/2008JC005131.

Chelton, D., M. Schlax, and R. Samelson, 2011: Global observations of nonlinear mesoscale eddies. *Prog. Oceanogr.*, **91**, 167–216, doi:10.1016/j.pocean.2011.01.002.

Dewar, W., 2003: Nonlinear midlatitude ocean adjustment. *J. Phys. Oceanogr.*, **33**, 1057–1081, doi:10.1175/1520-0485(2003)033<1057:NMOA>2.0.CO;2.

Dijkstra, H., and M. Ghil, 2005: Low-frequency variability of the large-scale ocean circulations: A dynamical systems approach. *Rev. Geophys.*, **43**, RG3002, doi:10.1029/2002RG000122.

Gan, J., H. Li, E. Curchitser, and D. Haidvogel, 2006: Modeling South China Sea circulation: Response to seasonal forcing regimes. *J. Geophys. Res.*, **111**, C06034, doi:10.1029/2005JC003298.

Haidvogel, D., J. McWilliams, and P. Gent, 1992: Boundary current separation in a quasigeostrophic, eddy-resolving ocean circulation model. *J. Phys. Oceanogr.*, **22**, 882–902, doi:10.1175/1520-0485(1992)022<0882:BCSIAQ>2.0.CO;2.

Helfrich, K., and L. Pratt, 2003: Rotating hydraulics and upstream basin circulation. *J. Phys. Oceanogr.*, **33**, 1651–1663, doi:10.1175/2383.1.

Hsin, Y., B. Qiu, T. Chiang, and C. Wu, 2013: Seasonal to interannual variations in the intensity and central position of the surface Kuroshio east of Taiwan. *J. Geophys. Res. Oceans*, **118**, 4305–4316, doi:10.1002/jgrc.20323.

Hu, D., and Coauthors, 2015: Pacific western boundary currents and their roles in climate. *Nature*, **522**, 299–308, doi:10.1038/nature14504.

Hu, J., H. Kawamura, H. Hong, and Y. Qi, 2000: A review on the currents in the South China Sea: Seasonal circulation, South China Sea warm current and Kuroshio intrusion. *J. Oceanogr.*, **56**, 607–624, doi:10.1023/A:1011117531252.

Hughes, C., and B. de Cuevas, 2001: Why western boundary currents in realistic oceans are inviscid: A link between form stress and bottom pressure torques. *J. Phys. Oceanogr.*, **31**, 2871–2885, doi:10.1175/1520-0485(2001)031<2871:WWBCIR>2.0.CO;2.

Ierley, G., 1987: On the onset of inertial recirculation in barotropic general circulation models. *J. Phys. Oceanogr.*, **17**, 2366–2374, doi:10.1175/1520-0485(1987)017<2366:OTOOIR>2.0.CO;2.

Isobe, A., and S. Imawaki, 2002: Annual variation of the Kuroshio transport in a two-layer numerical model with a ridge. *J. Phys. Oceanogr.*, **32**, 994–1009, doi:10.1175/1520-0485(2002)032<0994:AVOTKT>2.0.CO;2.

Jiang, S., F. Jin, and M. Ghil, 1995: Multiple equilibria and aperiodic solutions in a wind-driven, double-gyre, shallow-water model. *J. Phys. Oceanogr.*, **25**, 764–786, doi:10.1175/1520-0485(1995)025<0764:MEPAAS>2.0.CO;2.

Jing, C., and L. Li, 2003: An initial note on quasi-stationary, cold-core Lanyu eddies southeast off Taiwan Island. *Chin. Sci. Bull.*, **48**, 2101–2107, doi:10.1360/03wd0012.

Kida, S., J. Price, and J. Yang, 2008: The upper-oceanic response to overflows: A mechanism for the Azores Current. *J. Phys. Oceanogr.*, **38**, 880–895, doi:10.1175/2007JPO3750.1.

——, J. Yang, and J. Price, 2009: Marginal sea overflows and the upper-ocean interaction. *J. Phys. Oceanogr.*, **39**, 387–403, doi:10.1175/2008JPO3934.1.

Kuehl, J., and V. Sheremet, 2009: Identification of a cusp catastrophe in a gap-leaping western boundary current. *J. Mar. Res.*, **67**, 25–42, doi:10.1357/002224009788597908.

Lan, J., N. Zhang, and Y. Wang, 2013: On the dynamics of the South China Sea deep circulation. *J. Geophys. Res. Oceans*, **118**, 1206–1210, doi:10.1002/jgrc.20104.

Liang, W., T. Tang, Y. Yang, M. Ko, and W. Chuang, 2003: Upper-ocean currents around Taiwan. *Deep-Sea Res. II*, **50**, 1085–1105, doi:10.1016/S0967-0645(03)00011-0.

——, Y. Yang, T. Tang, and W. Chuang, 2008: Kuroshio in the Luzon Strait. *J. Geophys. Res.*, **113**, C08048, doi:10.1029/2007JC004609.

Liu, Q., A. Kaneko, and J. Su, 2008: Recent progress in studies of the South China Sea circulation. *J. Oceanogr.*, **64**, 753–762, doi:10.1007/s10872-008-0063-8.

Lu, J., and Q. Liu, 2013: Gap-leaping Kuroshio and blocking westward-propagating Rossby wave and eddy in the Luzon Strait. *J. Geophys. Res. Oceans*, **118**, 1170–1181, doi:10.1002/jgrc.20116.

Marshall, D., and J. Marshall, 1992: Zonal penetration scale of midlatitude oceanic jets. *J. Phys. Oceanogr.*, **22**, 1018–1032, doi:10.1175/1520-0485(1992)022<1018:ZPSOMO>2.0.CO;2.

Marshall, J., and A. Nurser, 1986: Steady, free circulation in a stratified quasigeostrophic ocean. *J. Phys. Oceanogr.*, **16**, 1799–1813, doi:10.1175/1520-0485(1986)016<1799:SFCIAS>2.0.CO;2.

McCalpin, J., and D. Haidvogel, 1996: Phenomenology of the low-frequency variability in a reduced-gravity, quasigeostrophic double-gyre model. *J. Phys. Oceanogr.*, **26**, 739–752, doi:10.1175/1520-0485(1996)026<0739:POTLFV>2.0.CO;2.

McWilliams, J., 1977: A note on a consistent quasigeostrophic model in a multiply connected domain. *Dyn. Atmos. Oceans*, **1**, 427–441, doi:10.1016/0377-0265(77)90002-1.

Mu, L., L. Zhong, L. Hua, and J. Song, 2011: Low-frequency variability of a semi-closed sea induced by the circulation in an adjacent ocean in a wind-driven, quasi-geostrophic, eddy-resolving simulation. *Ocean Dyn.*, **61**, 1459–1473, doi:10.1007/s10236-011-0443-2.

Nakano, H., H. Tsujino, and R. Furue, 2008: The Kuroshio current system as a jet and twin "relative" recirculation gyres embedded in the Sverdrup circulation. *Dyn. Atmos. Oceans*, **45**, 135–164, doi:10.1016/j.dynatmoce.2007.09.002.

Nan, F., H. Xue, F. Chai, L. Shi, P. Shi, and P. Guo, 2011: Identification of different types of Kuroshio intrusion into the South China Sea. *Ocean Dyn.*, **61**, 1291–1304, doi:10.1007/s10236-011-0426-3.

——, ——, and F. Yu, 2015: Kuroshio intrusion into the South China Sea: A review. *Prog. Oceanogr.*, **137**, 314–333, doi:10.1016/j.pocean.2014.05.012.

Pedlosky, J., 1987: *Geophysical Fluid Dynamics*. 2nd ed. Springer-Verlag, 710 pp.

——, 1996: *Ocean Circulation Theory*. Springer-Verlag, 452 pp.

Qiu, B., 2001: Kuroshio and Oyashio Currents. *Encyclopedia of Ocean Sciences*, Academic Press, 1413–1425, doi:10.1006/rwos.2001.0350.

——, S. Chen, and N. Schneider, 2016: Inter-decadal modulations in the dynamical state of the Kuroshio Extension system: 1905-2015. *CLIVAR Exchanges*, No. 69, International CLIVAR Project Office, Southampton, United Kingdom, 6–9.

Risien, C., and D. Chelton, 2008: A global climatology of surface wind and wind stress fields from eight years of QuikSCAT scatterometer data. *J. Phys. Oceanogr.*, **38**, 2379–2413, doi:10.1175/2008JPO3881.1.

Sheremet, V., 2001: Hysteresis of a western boundary current leap across a gap. *J. Phys. Oceanogr.*, **31**, 1247–1259, doi:10.1175/1520-0485(2001)031<1247:HOAWBC>2.0.CO;2.

Stommel, H., 1948: The westward intensification of wind-driven ocean currents. *Eos, Trans. Amer. Geophys. Union*, **29**, 202–206, doi:10.1029/TR029i002p00202.

Sun, S., L. Wu, and B. Qiu, 2013: Response of the inertial recirculation to intensified stratification in a two-layer quasi-geostrophic ocean circulation model. *J. Phys. Oceanogr.*, **43**, 1254–1269, doi:10.1175/JPO-D-12-0111.1.

Taguchi, B., S. Xie, N. Schneider, M. Nonaka, H. Sasaki, and Y. Sasai, 2007: Decadal variability of the Kuroshio Extension: Observations and an eddy-resolving model hindcast. *J. Climate*, **20**, 2357–2377, doi:10.1175/JCLI4142.1.

Wang, D., and Coauthors, 2013: Progress of regional oceanography study associated with western boundary current in the South China Sea. *Chin. Sci. Bull.*, **58**, 1205–1215, doi:10.1007/s11434-012-5663-4.

Wang, G., S. Xie, T. Qu, and R. Huang, 2011: Deep South China Sea circulation. *Geophys. Res. Lett.*, **38**, L05601, doi:10.1029/2010GL046626.

Waterman, S., and S. Jayne, 2011: Eddy-mean flow interaction in the along-stream development of a western boundary current jet: An idealized model study. *J. Phys. Oceanogr.*, **41**, 681–707, doi:10.1175/2010JPO4477.1.

Wu, C., H. Lu, and S. Chao, 2008: A numerical study on the formation of upwelling off northeast Taiwan. *J. Geophys. Res.*, **113**, C08025, doi:10.1029/2007JC004697.

——, Y. Hsin, T. Chiang, Y. Lin, and I. Tsui, 2014: Seasonal and interannual changes of the Kuroshio intrusion onto the East China Sea Shelf. *J. Geophys. Res. Oceans*, **119**, 5039–5051, doi:10.1002/2013JC009748.

Xue, H., F. Chai, N. Pettigrew, D. Xu, M. Shi, and J. Xu, 2004: Kuroshio intrusion and the circulation in the South China Sea. *J. Geophys. Res.*, **109**, C02017, doi:10.1029/2002JC001724.

Yang, J., and J. Price, 2007: Potential vorticity constraint on the flow between two basins. *J. Phys. Oceanogr.*, **37**, 2251–2266, doi:10.1175/JPO3116.1.

Yasuda, I., 2003: Hydrographic structure and variability in the Kuroshio–Oyashio transition area. *J. Oceanogr.*, **59**, 389–402, doi:10.1023/A:1025580313836.

Zhong, L., L. Hua, and D. Luo, 2016: The eddy–mean flow interaction and the intrusion of western boundary current into the South China Sea–type basin in an idealized model. *J. Phys. Oceanogr.*, **46**, 2493–2527, doi:10.1175/JPO-D-15-0220.1.